Harmonic content and time variation of electron energy distributions in high-plasma-density, low-pressure inductively coupled discharges

Alex V. Vasenkov[a] and Mark J. Kushner[b]
University of Illinois, Department of Electrical and Computer Engineering, 1406 West Green Street, Urbana, Illinois 61801

(Received 28 March 2003; accepted 23 May 2003)

Plasma kinetics models which are commonly used to model rf discharges often produce electron energy distributions (EEDs) averaged over the rf cycle. In doing so, the time dynamics of the EEDs are lost. In this article we describe a technique to recover these time dynamics by using an ''on-the-fly'' (OTF) Monte Carlo method. The OTF method directly computes the harmonic content of the EEDs using Fourier transform techniques during advancement of the trajectories of pseudoelectrons. The OTF method was incorporated into a two-dimensional plasma equipment model to investigate the harmonic content of the EEDs and their time dependencies in inductively coupled low-pressure ($\leqslant$10 mTorr) and low-frequency ($\leqslant$16 MHz) plasmas sustained in Ar. The computational results demonstrated that the second harmonic dominates the time dynamics of the EEDs, and that this harmonic content mostly occurs at higher energies. The harmonic content at low energies is significant only in the electromagnetic skin layer. We also found that the time evolution of the second harmonic of the EED involves the simultaneous transit of several pulses in energy and space. These pulses are attributed to the nonlinear Lorentz force resulting from the rf magnetic field.
 [DOI: 10.1063/1.1592630]

I. INTRODUCTION

Inductively coupled plasma (ICP) sources are widely used for etching and deposition in microelectronics fabrication due to their high ionization efficiencies producing high electron and ion densities ($>10^{10}$ cm^{-3}).[1–5] These plasma sources are typically used at low pressures ($<$10's mTorr) and frequencies ($<$10's MHz) to facilitate collisionless ion transport through the sheath, reduce capacitive coupling and manage transmission line effects.[6,7] In this regime, nonlinear electron transport resulting from second harmonic and Pondermotive forces is significant.[5,8–12]

The physics of nonlinear electron transport in ICPs is complex and is a current topic of research. For example, Godyak *et al.* observed large electrical potentials in ICPs at the second harmonic when nonlinear processes dominate over the linear acceleration of electrons by the inductive electric field.[13] This potential is generated by the rf Hall effect, produced by the nonlinear Lorentz force (NLF), $\mathbf{v}\times\mathbf{B}$, resulting from the radial component of the rf magnetic field and azimuthal component of the electron velocity. As such, the NLF axially accelerates electrons at 2ω, where ω is the fundamental frequency of the electric field. Piejak and Godyak derived analytical expressions for the second harmonic and Pondermotive forces acting on electrons in ICP discharges.[9] They found that these forces scale as $1/(\nu_e\omega)$ in the highly collisional case when $\nu_e \gg \omega$, and as $1/\omega^2$ in the collisionless case when $\nu_e \ll \omega$, where ν_e is the collision frequency averaged over the electron energy distribution (EED).[9] Tomographic measurements of phase-resolved optical emission from ICPs in Ar and O_2 by Makabe and coworkers had significant harmonic content produced, in part, by these nonlinear Lorentz forces.[5,14,15] For example, their measurements of net excitation rates as a function of radius showed two maxima during the rf cycle resulting from $\mathbf{E}\times\mathbf{B}_{rf}$ drift in the quasi-dc radial electrostatic field.[14] Sankaran and Kushner numerically investigated the time dependence of excitation rates in low-pressure ICPs sustained in Ar/N_2.[12] They found that even harmonics dominate the source functions for inelastic high threshold processes as modulation of the EED at higher energies is more likely than at thermal energy. The harmonic content of excitation in ICPs was found to be critically sensitive to pressure and driving frequency, which ultimately determine the ratio $\gamma = \nu_e/\omega$.

In this article the harmonic content of EEDs in low pressure ICPs is discussed. The ''on-the-fly'' (OTF) Monte Carlo technique, originally developed to calculate the harmonic moments of EEDs, was adapted to obtain pure harmonics of EEDs and, subsequently, to reconstruct their time dependence. It was observed that when the skin layer is anomalous, the high energy structure of the EED is modulated at 2ω, in large part due to axial acceleration by the NLF. Under select conditions, pulses of energetic electrons are launched across the reactor, of which many could be in flight at any given time. The model is described in Sec. II. The results from our parametric study are presented and discussed in Sec. III. Concluding remarks are in Sec. IV.

II. DESCRIPTION OF THE MODEL

In this section the OTF method for investigating the harmonic content and time dependence of the EEDs in low-

[a]Permanent address: Institute of Thermophysics, Novosibirsk, 630090, Russia; electronic mail: vasenkov@uiuc.edu
[b]Electronic mail: mjk@uiuc.edu

pressure plasmas is described. By adapting the OTF method discussed in Ref. 12, statistics are collected in a Monte Carlo simulation for the harmonic coefficients of the EEDs as opposed to collecting statistics on the time dependence of the EEDs. The OTF technique was implemented in the Electron Monte Carlo Simulation (EMCS) of the two-dimentional Hybrid Plasma Equipment Model (HPEM).[16] A brief description of the HPEM will be given followed by a description of the OTF method.

The HPEM, described in detail in Ref. 16 and references therein, consisting of three major modules, was developed to investigate low temperature, low pressure plasma phenomena. The Electromagnetic Module (EMM) is used to calculate rf magnetic and electric fields by solving Maxwell equations. These fields are than used in the Electron Energy Transport Module (EETM) where electron transport coefficients and source functions are calculated. These functions are obtained using either the EMCS or by solving an electron energy equation coupled with a two-term solution of Boltzmann's equation. In this study, the EMCS was used to produce the kinetic transport properties required for the OTF method. Results from the EETM are transferred to the Fluid-Chemical Kinetics Module (FKM), which solves the continuity, momentum and energy equations for densities and temperatures of neutrals and charged species, and Poisson's equation for the electrostatic potential. A drift diffusion formalism is used for the electron continuity equation to enable an implicit solution of Poison's equation. The modules are iterated until a converged solution is obtained.

A detailed description of the EMCS and of the OTF method can be found in Refs. 12 and 17. The simulation starts by initially distributing electron pseudoparticles in coordinate and velocity space using initial estimates for electron density and temperature. Following initialization, the trajectories of the pseudoparticles are advanced through free flight acceleration or motion interrupted by collisions. Between these collisions the trajectories of the pseudoparticles are advanced according to the Lorentz equation using electromagnetic fields from the EMM and electrostatic fields from the FKM. The modeling of collisions over a wide range of collision frequency, produced primarily by changes in electron energy, is made tractable by the use of a null-collision technique. This is accomplished by adding what appears to be fictitious processes known as null collisions such that the total collision frequency appears to be constant. Electron–electron collisions, which significantly affect thermal electron motion, are treated separately from other events since the frequency of these collisions depends on the relative velocity of colliding electrons. These collisions are modeled using a test particle method and particle-mesh algorithms.[16]

Statistics which produce the spatially dependent, time averaged EEDs are collected on every time step in the EMCS by binning pseudoparticles using a two-dimensional mesh for spatial locations (separately uniform in radius and height) and a one-dimensional nonuniform mesh for energy. The mesh for energy usually has smaller width bins at lower energies to resolve more the complex structure of cross sections and EEDs, and larger widths at higher energies where the cross sections and the EEDs are smoother functions of energy. At every time step the raw statistics, F_{il} which eventually produce the EEDs, are updated as

$$F_{il} \rightarrow F_{il} + \sum_j \left\{ w_j \Delta t_j \delta[(\varepsilon_i \pm \tfrac{1}{2}\Delta\varepsilon_i) - \varepsilon_j] \sum_k \alpha_k \times \delta[(\mathbf{r}_{l+k} \pm \tfrac{1}{2}\Delta\mathbf{r}_{l+k}) - \mathbf{r}_j] \right\}, \quad (1)$$

where i and l are the energy and spatial indices, δ is the delta function and the summations are over j particles and k neighboring mesh cells. ε_j and $\mathbf{r}_j$ are the energy and location of the jth particle, and $\Delta\varepsilon_i$ and $\Delta\mathbf{r}_k$ are the energy and the mesh cell width. w_j is a pseudoparticle dependent weighting which accounts for the number of electrons the pseudoparticle represents and Δt_j is the previous time step. α_k is a weighting for finite-sized-particle accounting.[18] At the end of given iteration through the EMCS, the EEDs, f_{il}, are obtained from the raw statistics F_{il} by normalizing

$$W_l \sum_i F_{il} = \sum_i f_{il} \varepsilon_i^{1/2} \Delta\varepsilon_i = 1, \quad (2)$$

where W_l is a spatially dependent factor. The f_{il} obtained at the end of the EMCS are then used to update electron-impact rate coefficients, optionally backaveraging with previous iterations, which are transferred to the FKM.

The just described method produces EEDs which are averaged over the rf cycle and so information about the time dependence of the EEDs is lost. To recover this information, the OTF method was adapted to compute the harmonic content, and so the time-dependence of the EEDs, using a Fourier transform technique. The alternative, binning particles by phase in the rf cycle and so explicitly recording the time-dependent EEDs, was not used because of the large computational and memory requirements. The OTF method filters higher frequency noise in the EEDs by selectively computing lower order Fourier coefficients. Direct time domain techniques of resolving the time dependence would require larger numbers of particles or larger numbers of rf cycles of recording to suppress such noise.

The statistics for raw complex Fourier coefficients are collected similarly to those for time-averaged EEDs. For example, for the nth harmonic

$$\Psi_{il}^n \rightarrow \Psi_{il}^n + \sum_j \left\{ w_j \Delta t_j \exp(in\omega t_j) \delta[(\varepsilon_i \pm \tfrac{1}{2}\Delta\varepsilon_i) - \varepsilon_j] \times \sum_k \alpha_k \delta[(\mathbf{r}_{l+k} \pm \tfrac{1}{2}\Delta\mathbf{r}_{l+k}) - \mathbf{r}_j] \right\}. \quad (3)$$

This expression differs from Eq. (1) by the complex time-dependent factor $\exp(in\omega t_j)$ which accounts for the time evolution of the EEDs. At the end of a given iteration the amplitude and phase of the nth harmonic are obtained from the Fourier coefficients by

$$\Phi_{il}^n = \Psi_{il}^n / W_l, \qquad \varphi_{il}^n = \mathrm{Im}[\Psi_{il}^n] / \mathrm{Re}[\Psi_{il}^n], \quad (4)$$

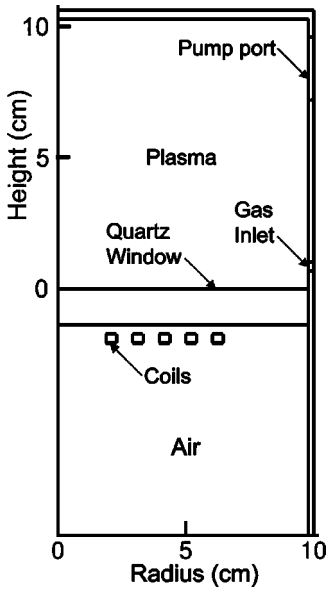

FIG. 1. Schematic of the cylindrically symmetric ICP reactor.

where W_l is the normalization factor from Eq. (2). The time dependence for the nth harmonic of the EEDs is then reconstructed from

$$f_{il}^n = \Phi_{il}^n \sin(n\omega t + \varphi_{il}^n), \tag{5}$$

where the zero harmonic f_{il}^0 is equivalent to the time-averaged EED, $f(\varepsilon_i, r_l)$, determined from Eq. (2). The time dependence of the EEDs is obtained by summing all available harmonics

$$f(\varepsilon_i, r_l, t) = \max\left[0, \sum_{n=1}^{N} f_{il}^n\right]. \tag{6}$$

The harmonics having n different than zero alternate between having positive and negative values depending on their phase. The EED must always be positive because it is the probability of having an electron of a given energy and space coordinates at a given time. As noise in the EMCS sometimes result in the sum of phase weighted amplitudes being negative, the maximum in Eq. (6) is applied.

III. HARMONIC CONTENT OF EEDs

In this section the time dependence of EEDs and their harmonics in ICPs sustained in Ar will be discussed. The electron-impact cross sections, heavy particle reaction rate coefficients, and the geometry of the ICP reactor used in this investigation are the same as in Ref. 17. This geometry is shown in Fig. 1. Briefly, the ICP plasma is produced in a cylindrically symmetric chamber, 10 cm in radius and 10.75 cm tall. The rf antenna is a five turn coil set atop a quartz window 1.27 cm thick. Typical plasma parameters for the base case conditions (10 mTorr, 100 W, 6.78 MHz) are shown in Fig. 2. A peak electron density about 2×10^{11} cm^{-3} occurs at the center of the reactor as low-energy electrons pool from the plasma edges to the center where the electric potential peaks. A peak in the rate of ionization is located at the edge of skin depth where the tail of the EED is

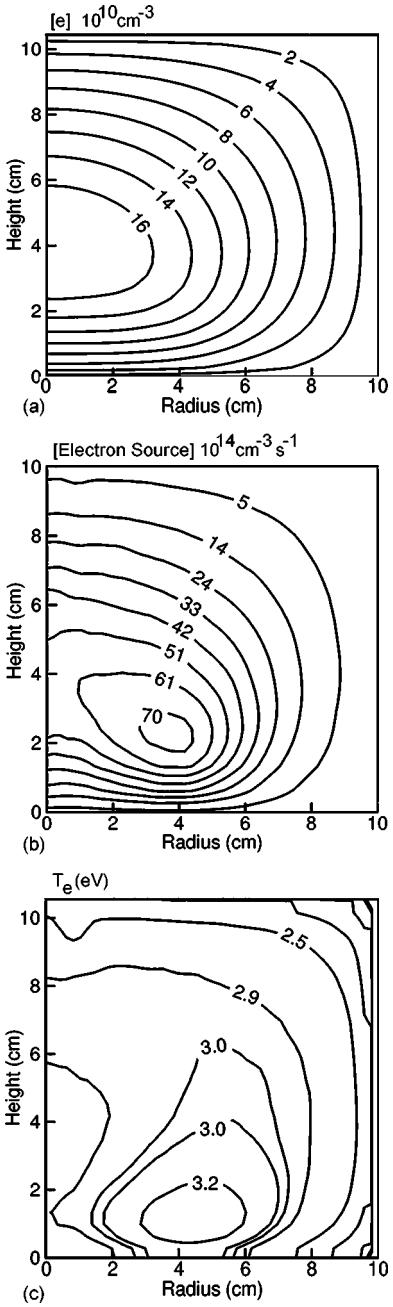

FIG. 2. Plasma parameters for the base case conditions (10 mTorr, 100 W, 6.78 MHz). (a) Plasma density, (b) electron impact ionization source function, and (c) electron temperature. The ionization source peaks at the edge of the skin layer.

largest in magnitude.[11,17] The classical collisionless skin depth, $\delta = (m/\mu_0 e^2 n_e)$, where μ_0 is the vacuum permeability, is about 2 cm for the base case conditions. The electron temperature T_e peaks in the skin layer, where electrons are strongly heated by the large rf fields. In the bulk plasma, T_e is lower as electrons transfer their energy to the gas by collisions. The mild gradients in T_e result from the efficient conduction of thermal energy across the reactor by electron–electron (e–e) collisions. Since in the bulk plasma beyond the skin depth, direct electron heating by the electromagnetic field is small, electron thermal conduction dominates heating of low energy electrons. This effect is clearly demonstrated

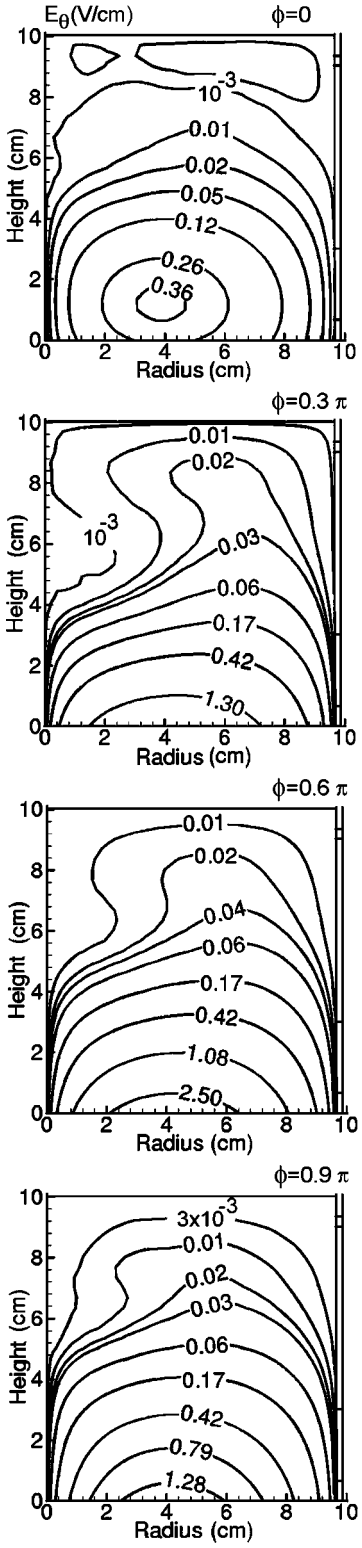

FIG. 3. E_θ (V/cm) for the base case conditions (10 mTorr, 100 W, 6.78 MHz) for different phases during the rf cycle. (a) $\phi=0$, (b) $\phi=0.3\ \pi$, (c) $\phi=0.6\ \pi$, (d) $\phi=0.9\ \pi$. Dephasing of thermal electrons produce destructively interfering electric fields which result in nodes in the penetrating inductively coupled field.

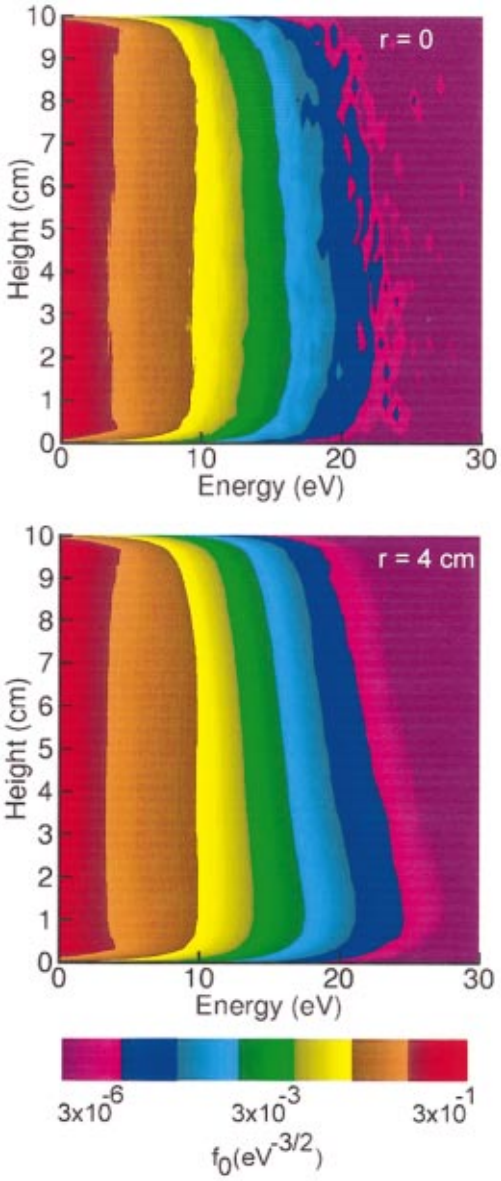

FIG. 4. (Color) The time-averaged EEDs (units $eV^{-3/2}$) for the base case conditions (10 mTorr, 100 W, 6.78 MHz) for (top) $r=0$ and (bottom) $r=4$ cm. The time averaged EED is the same as the f_0 component. On axis, there is little accentuation of the tail of the EED in the skin layer. At mid radius, the EED is enhanced at high energies in the skin layer, extending into the bulk plasma, a result of NLF. The EEDs are fairly uniform as a function of height at low energy due to thermalization by e–e collisions.

by removing e–e collisions from the simulation. Without e–e collisions, T_e there is a significant minimum in the center of the plasma where low energy electrons are trapped at the peak of the plasma potential.

The time evolution of the azimuthal electric field E_θ for the base case conditions during the first half of the rf cycle is shown in Fig. 3. E_θ exponentially decreases in the skin depth with distance from the coils for all phases of the rf cycle. Close to the opposite wall, E_θ has extrema and nodes resulting from thermal electron motion which generates current sources interfering or reinforcing the local electric field.[10,17,19] These currents, transferred by electron thermal motion, are too small to significantly perturb the rf fields in the skin layer, where E_θ is large, whereas these currents have measurable effects on the electric field beyond the classical skin layer where E_θ has decayed to smaller values.

Time-averaged EEDs, which are the same as the 0th harmonic, are shown in Figs. 4 and 5 as a function of height for

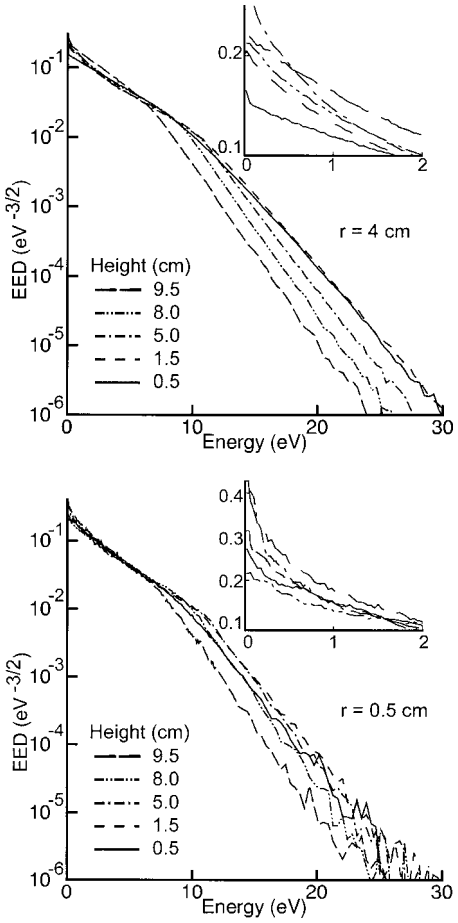

FIG. 5. The time-averaged EEDs (units $eV^{-3/2}$) for the base case conditions as a function of energy for fixed axial and radial positions (top) $r=4$ cm (bottom) $r=0.5$ cm. At $r=4$ cm, the tail of the EED is largest at the edge of the skin layer as a result of collisionless heating. The EED peaks at low energies in the bulk plasma. The EEDs at low energy on the axis weakly depend on height as high thermal conductivity due to e–e collisions reduces temperature gradients.

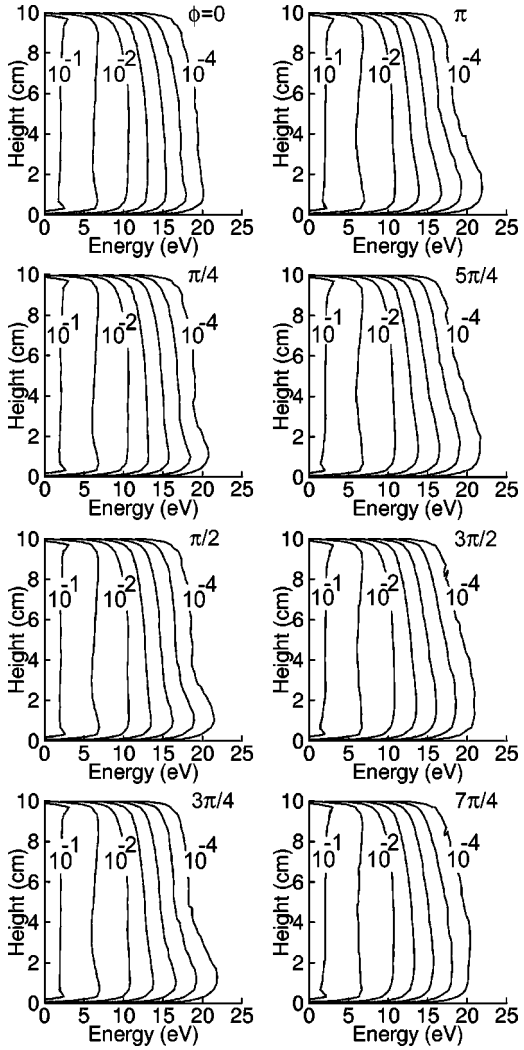

FIG. 6. EEDs (units $eV^{-3/2}$) for the base case conditions (10 mTorr, 100 W, 6.78 MHz) at $r=4$ cm for different phases during the rf cycle. The tail of the EED is enhanced in the skin layer followed by propagation of high energy electrons into the bulk plasma.

the base case conditions at two radial positions, near the axis at $r=0$ and $r=4$ cm. Due to the large electron-electron collision frequency in the middle of the reactor and the resulting efficient transfer of thermal energy, the distribution of low-energy electrons near $r=0$ is nearly axially uniform except near the coils and the far wall. The EED is depleted at low energies near surfaces as a consequence of pooling towards the center of the reactor where the plasma potential peaks and which traps low-energy electrons.[11] The electrons in the skin depth are dominantly collisionlessly heated. The contribution of Ohmic heating in the skin depth is small as electron mean free paths (≈ 2 cm at 10 eV) are comparable to the skin depth. In the bulk plasma, Ohmic heating is not an unreasonable approximation. The net power deposition obtained by assuming only Ohmic heating is only three times less than the total net power deposition in an ICP discharge sustained in Ar at 100 W and 10 mTorr.[20,21] The distribution of high-energy electrons on axis only slightly peaks at the edge of the skin layer. Electrons here are only indirectly affected by collisionless heating in the skin layer since E_θ is zero on the axis. These electrons are heated as a result of scattering of electrons from larger radii where the electric field is also larger, or by thermal conduction resulting from e–e collisions.

The EEDs show more evidence of acceleration in the skin layer at $r=4$ cm, where the amplitude of the electric field is large (≈ 3 V/cm). The largest fraction of high-energy electrons resides at the edge of the collisionless skin depth producing significant ionization in this region, as shown in Fig. 2(b). The tail of the EED decays with distance from the coils. Electrons having energies greater the plasma potential escape from the bulk plasma to the walls and electrons having energies greater than the first inelastic threshold at 11.6 eV dissipate their energy by collisions. Electrons with energies below the first inelastic threshold are nearly spatially uniform in the axial direction since they are trapped by the electrostatic potential and e–e collisions efficiently conduct electron energy, thereby smoothing the distribution function.

The time evolution of the EED for the base case as a function of height at $r=4$ cm when including six harmonics is shown in Fig. 6 for different phases in the rf cycle. The high-energy tail of the EEDs at $\phi=0$ is only moderately

enhanced in the skin layer as the electric field crosses zero. As the electric field increases in magnitude, the energy of electrons in the skin layer rapidly increases due to noncollisional heating. The EEDs at $\phi=\pi/4$ and $\phi=\pi/2$ are enhanced at high energies in the skin layer as the electric field increases but the tails of the EEDs are less affected deeper into the plasma. The increase in the azimuthal component of the velocity of electrons in the skin layer produces a corresponding increase in the Lorentz force which accelerates electrons out of the skin layer into the bulk plasma. As a result, the differences between the tails of EEDs in the skin layer and in the bulk plasma decrease as this axial force accelerates electrons out of the skin layer. The EEDs for $\phi=3\pi/4$ through $7\pi/4$ show this transition. As the phase crosses π, the electric field decelerates electrons in the skin layer producing a lowering of the tail of the EED. This process continues until $\phi=7\pi/4$ when the EED in the skin layer differs little from that in the bulk.

The amplitudes of the first four harmonics of the EEDs as a function of height are compared in Fig. 7 at $r=4$ cm. The amplitude of f_1 is nearly uniform as a function of height and is dominantly produced by electrostatically trapped electrons with energies below the plasma potential. Consequently, the peak of f_1/f_0 is only 0.1. The energy distribution of these electrons is practically time-independent as a consequence of their collective dephasing by e-neutral and e–e collisions. The second harmonic has the largest amplitude at both low and high energies producing a peak of $|f_2/f_0|\approx 0.5$ at $\varepsilon\approx 20$ eV. f_2 has large-scale structures in the skin layer which are formed as a result of collisionless electron acceleration. The third harmonic consists of low-amplitude structures which appear similar to the first harmonic as both are also largely determined by the trapped electrons. The amplitude of fourth harmonic is similar to the first and the third except in the skin layer where there is a maximum ($|f_4/f_0|\approx 0.2$ at $\varepsilon\approx 20$ eV) resulting from collisionless electron motion.

Since the nonlinear dynamics of the EEDs are dominated by the second harmonic, we will focus further discussion on its properties. The time dependence of f_2 for the base case conditions is shown in Figs. 8 and 9. The second harmonic has both positive (f_2^+) and negative (f_2^-) components. A large value of f_2^+ implies an abundance of electrons whose energy oscillates at the second harmonic relative to the time-averaged distribution, whereas a large value of f_2^- implies depletion of electrons having energy oscillating at 2ω relative to f_0. In analogy with semiconductor transport, f_2^- can be thought of as being produced by holes.

Electrons oscillating at 2ω are dominantly produced by noncollisional heating in the skin layer by E_θ generating a pulse of hot electrons near the dielectric. NLF forces then accelerate these electrons out of the skin layer into the bulk plasma. Pulses of such electrons propagate across the reactor dissipating in both energy and coherency. At any given time there could be many such pulses in transit. The ''life cycle'' of one such pulse can be viewed from Figs. 8 and 9 by following the f_2^+ dynamics. The behavior for phases $0<\phi<\pi$ is identical to that for phases $0<\phi<2\pi$ with the roles

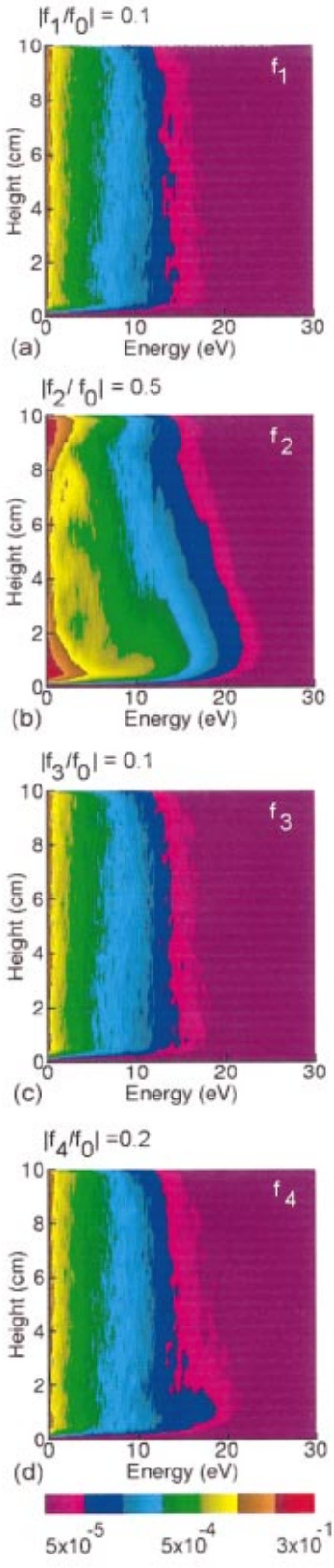

FIG. 7. (Color) Relative amplitudes of the first four harmonics as a function of height for the base case conditions (10 mTorr, 100 W, 6.78 MHz) at $r=4$ cm. (a) f_1/f_0, (b) f_2/f_0, (c) f_3/f_0, and (d) f_4/f_0. The maximum value of the harmonic amplitude is shown above each figure. The even harmonics have the largest amplitudes. The amplitudes of the odd harmonics are fairly uniform due to the large frequency of dephasing collisions.

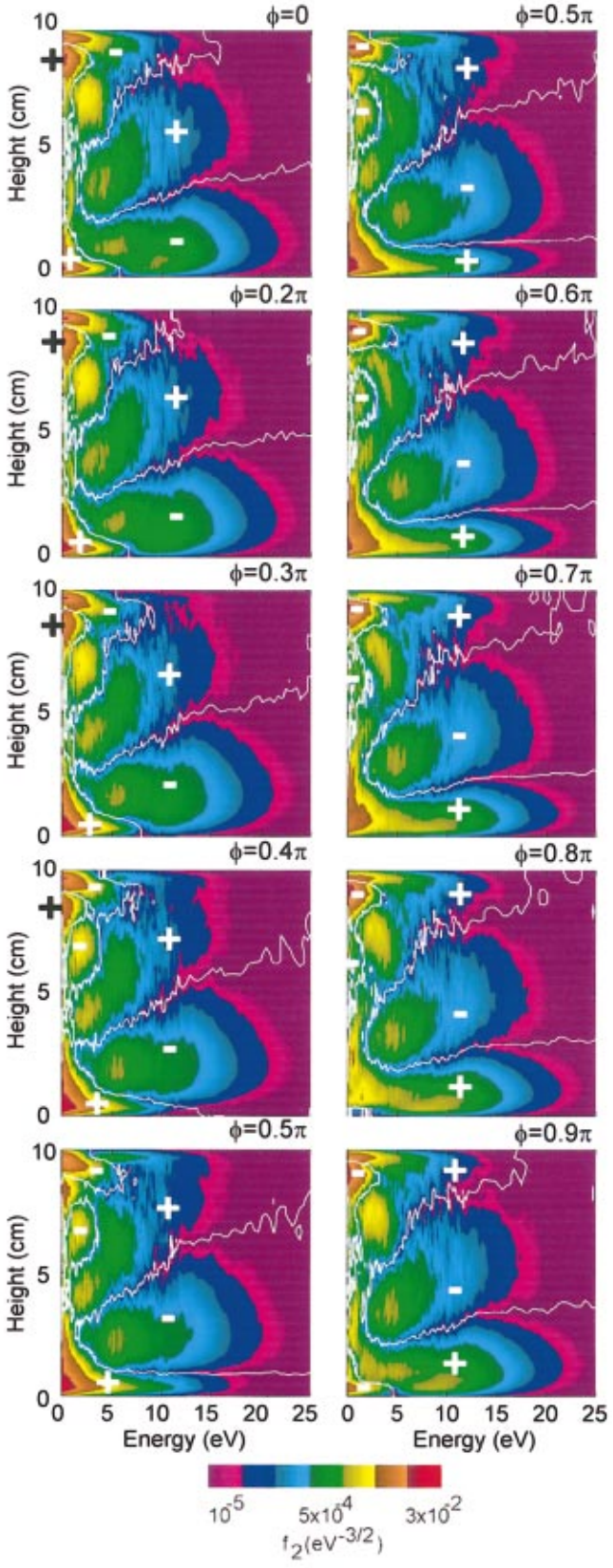

FIG. 8. (Color) The harmonic component f_2 for different phases ϕ during the rf cycle as a function of height at $r=4$ cm for the base case conditions (10 mTorr, 100 W, 6.78 MHz). Regions of the energy-height plane where f_2 is positive (f_2^+) or negative (f_2^-) are separated by the white contour line. Regions labeled "+" are occupied by f_2^+ for $0<\phi<\pi$ and by f_2^- for $\pi<\phi<2\pi$. Regions labeled "−" are occupied by f_2^- for $0<\phi<\pi$ and by f_2^+ for $\pi<\phi<2\pi$. Successive pulses of high energy electrons propagate across the reactor.

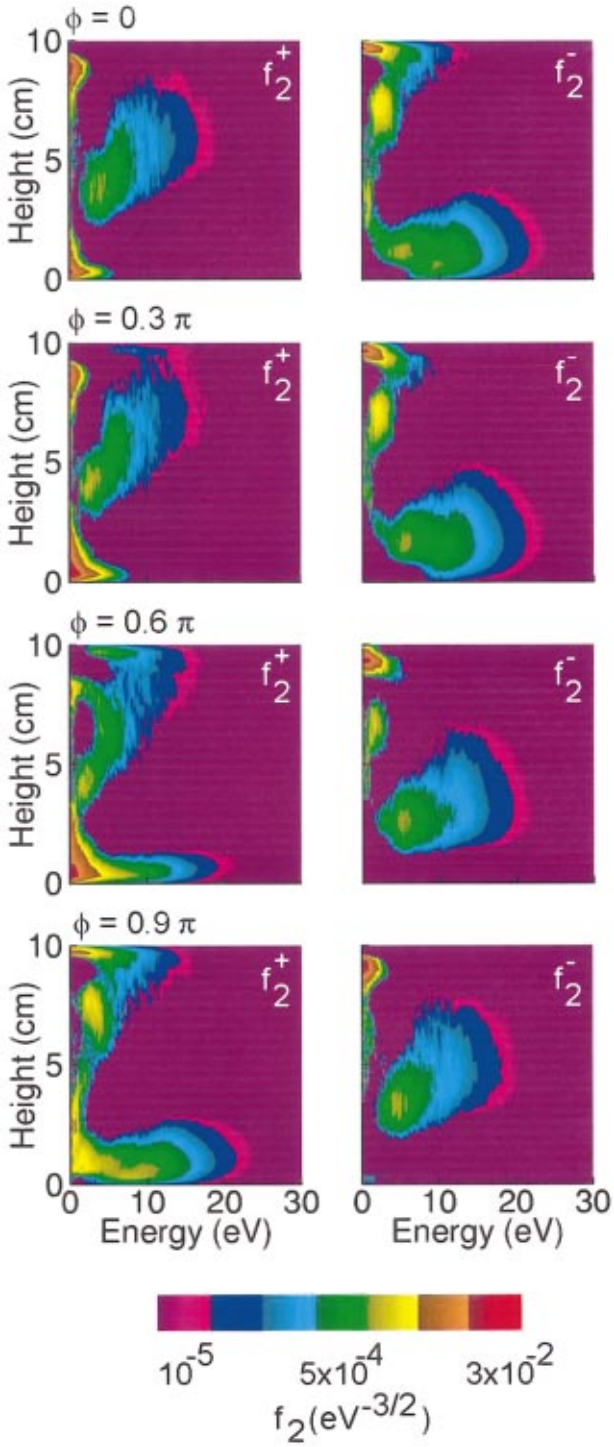

FIG. 9. (Color) f_2^+ and f_2^- as a function of height at $r=4$ cm for different phases in the rf cycle for the base case conditions (10 mTorr, 100 W, 6.78 MHz).

of f_2^+ and f_2^- reversed. Regions of the energy-height plane of Fig. 8 labeled "+" are occupied by f_2^+ during $0<\phi<\pi$ and f_2^- during $\pi<\phi<2\pi$. Those labeled "−" are occupied by and f_2^- during $0<\phi<\pi$ and by f_2^+ during $\pi<\phi<2\pi$. f_2^+ and f_2^- are separately shown in Fig. 9.

The origin of a pulse begins at phase $\phi=0$ with low energy f_2^+ electrons in the skin depth being accelerated by E_θ [lower left corner of (ε,z)]. As the cycle progresses,

these electrons are accelerated up the energy axis but do not propagate far in z as acceleration is parallel to the dielectric. By $\phi=0.5\pi$, a long tail to the f_2^+ EED has been generated in the skin layer. At this phase, Lorentz forces begin accelerating the f_2^+ electrons into the bulk plasma ($\phi=0.5\pi-0.9\pi$). The f_2^+ pulse "separates" from the skin layer at about $\phi=1.3\pi$ (the "−" region at $\phi=0.3\pi$) as the Lorentz force decreases and as E_θ changes sign to begin decelerating electrons in the skin layer. The separated f_2^+ pulse propagates across the reactor, progressively dephasing due to collisions (as indicated by the broadening in axial extent) and decreasing in energy (as indicated by the lowering in energy of the centroid of the pulse). The centroid of the f_2^+ pulse gains in energy even when leaving the skin layer as it is accelerated towards the maximum in the plasma potential and decelerates as the centroid passes the peak in the plasma potential and begins to climb the opposite presheath. After one complete rf cycle, the f_2^+ centroid is approximately at mid-reactor; and at $\phi=2.3\pi$ (the "+" region at $\phi=0.3\pi$) the leading edge of the f_2^+ pulse intersects the opposite wall. The slope of the f_2^+ pulse in the (ε,z) plane steepens with time as high energy electrons with longer mean-free paths outpace the lower energy electrons.

When the pulse reaches the opposite wall, the f_2^+ electrons are decelerated in the sheath, forming a pool of low energy electrons [top left corner of (ε,z)]. This deceleration and pooling occurs over $\phi=2.4\pi$ to 3π (the "+" region for $\phi=0.4\pi-\pi$.). These electrons begin propagating back towards the peak in the plasma potential at the center of the reactor over $\phi=2.5\pi-3.5\pi$ (the "+" region for $\phi=0.5\pi-\pi$, and the "−" region for $\phi=0-0.5\pi$). This "return" pulse is rapidly dephased due to frequent elastic collisions (both electron-heavy particle and e–e).

By following the f_2^- dynamics ("−" during $\phi=0-\pi$, and "+" during $\phi=\pi-2\pi$) we track the depletion of electrons at the second harmonic, or the transport of electron holes. For example, as the f_2^+ pulse leaves the skin depth $\phi=1.3\pi$ ("−" at $\phi=0.3\pi$) f_2^- dominates in the skin layer, an indication of deceleration by E_θ and depletion by the Lorentz force. The depletion zone propagates into the bulk plasma, shadowing the f_2^+ pulse.

While the dynamics of high-energy electrons are largely determined by the rf fields in the skin layer, the transport of low-energy electrons is dominated by thermal diffusion and e–e collisions. Low-energy electrons generated by ionization at the edge of skin layer diffuse back towards the coils and periodically repopulate the skin layer. The proportion of these electrons is $S_e/(2\omega n_s)$, where S_e is the electron source at the edge of skin layer and n_s is the electron density in the skin layer. For the base conditions, about 5% of the electrons are repopulated in the skin layer by ionization during the portion of the cycle when the Lorentz force is weak. Once these thermal electrons enter the skin layer, they are heated by the rf electric field thereby initiating the large-scale structures formed in the skin layer. This electron recirculation in ICP discharges also has been observed experimentally[22] and predicted numerically.[23]

The time dependence of the EEDs at a reduced pressure and frequency (1 mTorr, 3.39 MHz, 100 W) is shown in Figs. 10 and 11. By reducing the pressure, the mean-free path increases and collision frequency decreases. The electron dynamics are essentially collisionless everywhere as the anomalous skin depth is comparable to the height of the reactor. For these conditions collisionless heating is an order

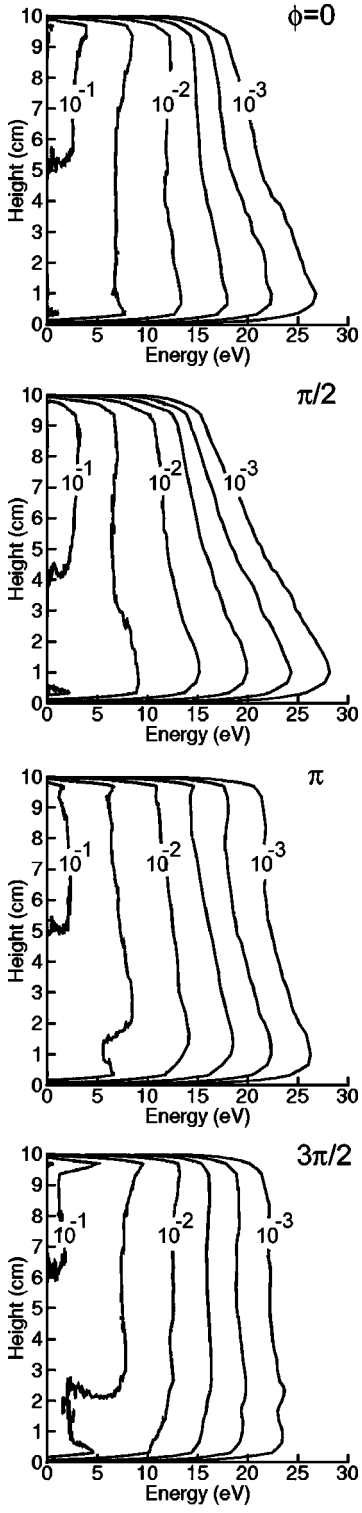

FIG. 10. EEDs as a function of height at $r=4$ cm at reduced pressure and frequency (1 mTorr, 100 W, 3.39 MHz) for different phases in the rf cycle. The lower pressure (longer mean-free paths) and lower frequency (larger rf magnetic fields) produces more pronounced harmonic modulation in the EEDs.

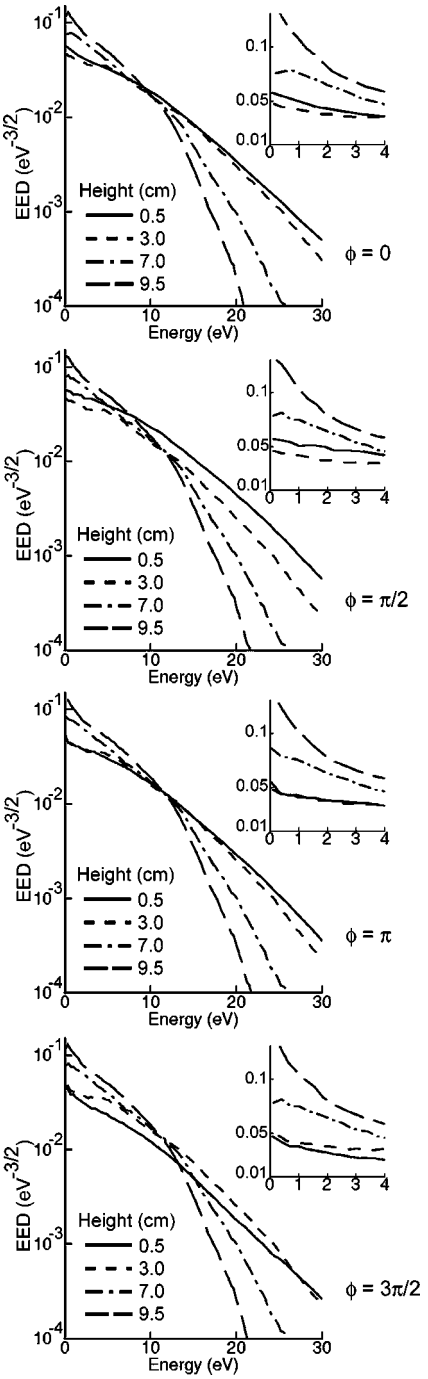

FIG. 11. EEDs as a function of energy for fixed axial positions at reduced pressure and frequency (1 mTorr, 100 W, 3.39 MHz), and $r=4$ cm for different phases in the rf cycle. The largest changes occur in the tail of EED as NLF mostly affects the motion of high energy electrons.

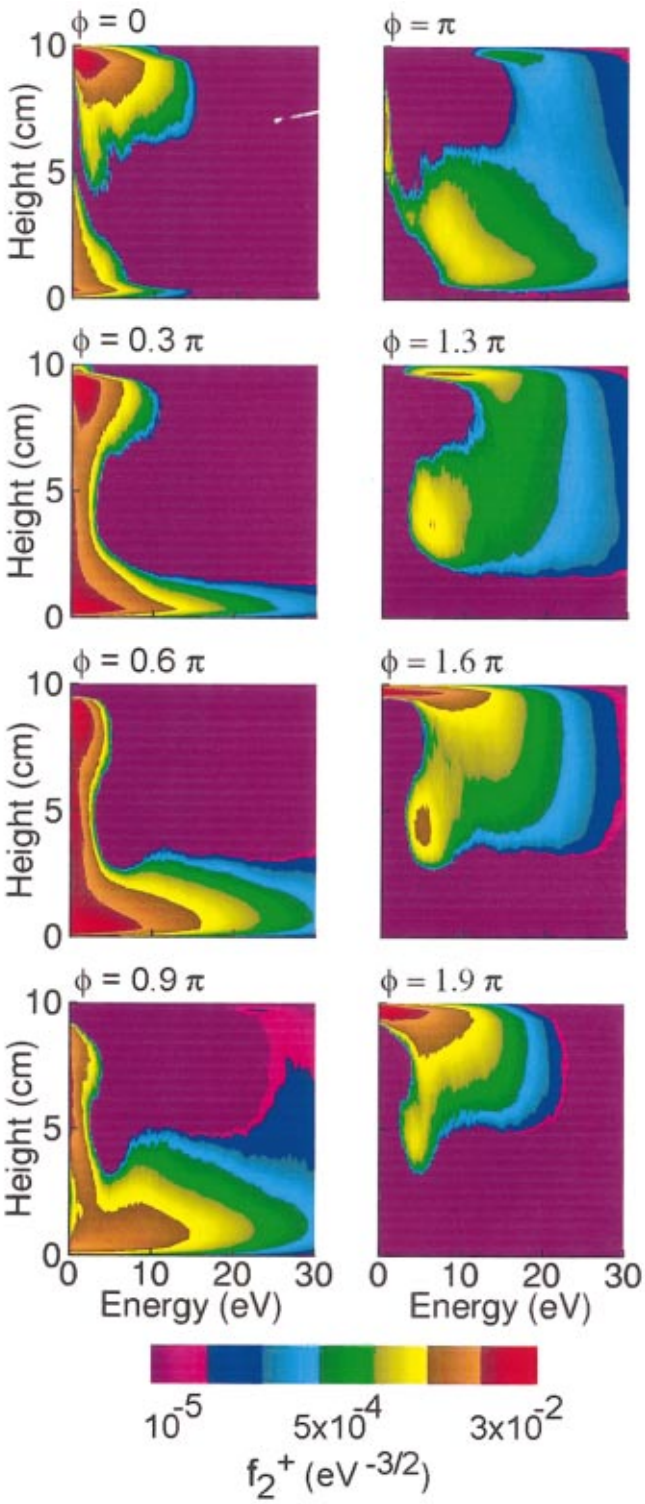

FIG. 12. (Color) f_2^+ as a function of height at $r=4$ cm at different phases during the rf cycle at a reduced pressure and frequency (1 mTorr, 100 W, 3.39 MHz). The lower pressure and larger NLF produces a pulse at the second harmonic which extends over a broader extent in the energy-height plane.

of magnitude larger than Ohmic heating.[20,21] Beginning prior to $\phi=0$ electrons are collisionlessly heated in the skin layer forming the EEDs at $\phi=0$ and $\phi=\pi/2$ which are depleted at low energies and enhanced at high energies. The high-energy electrons are accelerated out of the skin layer by the Lorentz force, which depletes the tail of the EEDs in the skin layer and increases the proportion of high-energy electrons in the bulk plasma for $\phi=\pi$ and $\phi=3\pi/2$. At the same time, the sheath at the opposite wall reflects electrons with energies below the plasma potential (16 eV) back into plasma forming a peak in the EEDs.

The time dependence of f_2 at 1 mTorr and 3.39 MHz is shown in Fig. 12. At this lower frequency the magnitude of the rf magnetic field is proportionately larger. Following the

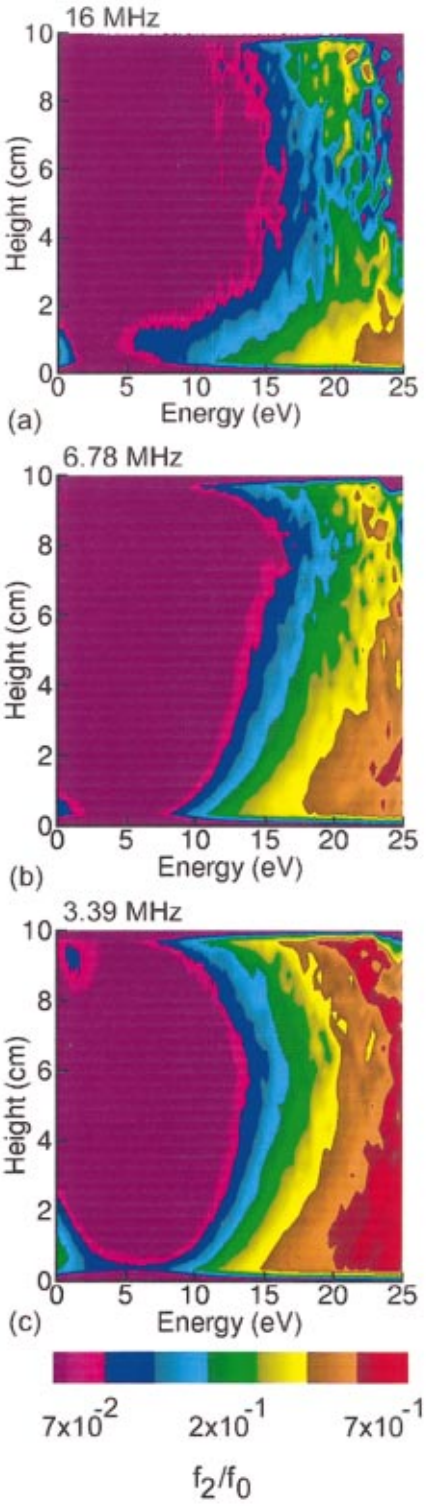

FIG. 13. (Color) The ratio of f_2/f_0 as a function of height and energy at $r=4$ cm for (a) 16, (b) 6.78, and (c) 3.39 MHz for otherwise the base case conditions (10 mTorr, 100 W). Larger modulations at the second harmonic occur at lower frequencies.

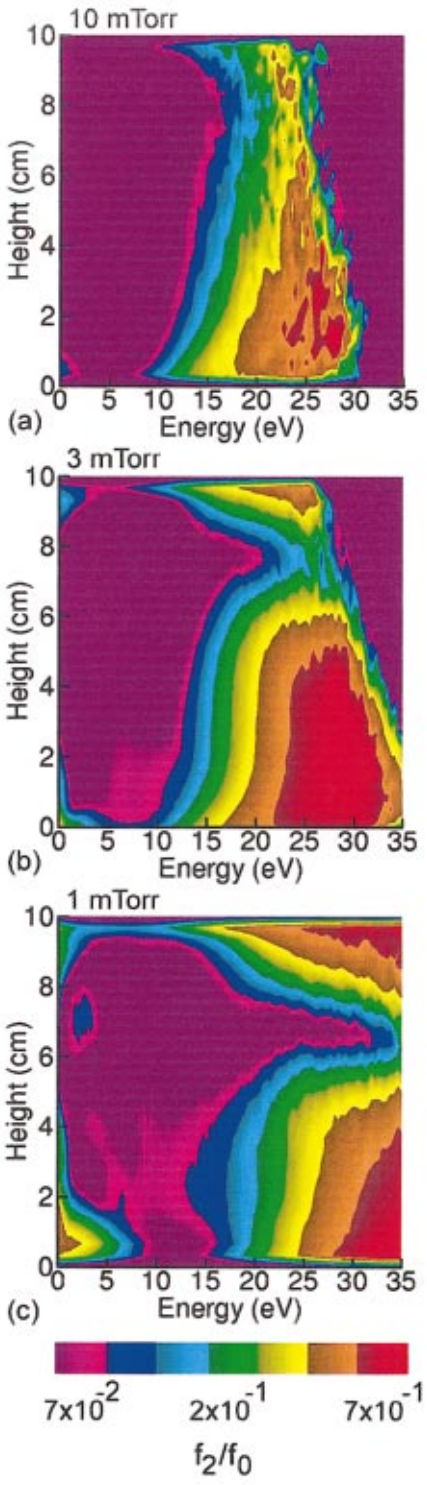

FIG. 14. (Color) The ratio of f_2/f_0 as a function of height and energy at $r=4$ cm for (a) 10, (b) 3, and (c) 1 mTorr for 6.78 MHz.

zero crossing of E_θ ($\phi=0$) electrons having diffused into the skin layer are rapidly accelerated to high energy in the nearly collisionless conditions and higher E/N at 1 mTorr. As the NLF begins to accelerate these electrons out of the skin layer ($\phi=0.6\pi$) the resulting pulse is more extended in both energy and axial extent than for the base case due to the lower collisionality. The higher energy electrons which outrace the bulk of the pulse reach the opposite sheath at $\phi \approx \pi$, decelerating by virtue of climbing the opposite sheath ($\phi=1.3\pi$). Those electrons which have energies less than the sheath potential and are not lost to the surface reverse direction and form a return pulse ($\phi=1.9\pi$). This approximately coincides in time to when the lower energy portion of the original pulse reaches the opposite wall. Due to the lower

collisionality, larger NLF and longer rf period at this lower pressure and frequency, there is generally only a single pulse in transit across the reactor, compared to the multiple pulses shown in Fig. 8 for a higher frequency and higher pressure.

The ratios f_2/f_0 for different frequencies but otherwise the base case conditions are shown in Fig. 13. Significant modulation of the EED at 2ω is indicated by large values of f_2/f_0. This modulation is largest at high energies and in the skin layer for all frequencies; and extends to greater heights as the frequency decreases. The larger harmonic content throughout the volume at lower frequencies results, in part, from the increase in the electromagnetic skin depth and increase in rf magnetic field which extends the region in which electrons are accelerated by the NLF. The larger harmonic content at higher energies results from the larger proportional contribution of NLF and longer mean-free paths. Electrons in the bulk plasma are dephased over shorter distances due to both electron-neutral and e–e collisions.

The ratios f_2/f_0 for different pressures but otherwise the base case conditions are shown in Fig. 14. As the pressure decreases, modulation of the EEDs produced by NLF in the skin depth extends to higher energies as the lower collisionality enables population of the tails of the EEDs. The apparent ''cutoff'' of f_2/f_0 at 10 mTorr results in part from the higher collisionality which dephases the electrons thereby decreasing f_2/f_0 and in part from the loss of higher energy electrons due to the lower plasma potential. As the plasma potential increases with decreasing pressure, a larger proportion of these electrons are retained and are reflected by the opposing sheath. This reflection is shown by the extension of f_2/f_0 down the energy axis at the top of the reactor.

IV. CONCLUDING REMARKS

The on-the-fly Monte Carlo technique, originally developed to investigate harmonic moments of EEDs was adapted to resolve the harmonic content of the EEDs, and, subsequently, to reconstruct their time dependence in low pressure ($\leqslant$10 mTorr) and low frequency ($\leqslant$16 MHz) ICPs sustained in Ar. It was observed that the second harmonic, f_2, dominates the frequency content of the EEDs and that these harmonics are mostly found at higher energies. The time evolution of f_2 can involve the simultaneous transit of several pulses in energy and space. These pulses in large part originate from the nonlinear Lorentz forces in the skin layer, increasing in intensity as the skin layer becomes more anomalous. As such the spatial width and energy range of the pulses increase with decreasing frequency and pressure. The dynamics of these pulses can be partially explained in terms of an electron recirculation process, during which low-energy electrons from the bulk plasma thermally diffuse into the skin layer followed by the noncollisional heating of these electrons by the large rf electric fields in the skin layer, and the nonlinear Lorentz force acceleration of hot electrons from the skin layer into the bulk plasma.

ACKNOWLEDGMENTS

This work was supported by the National Science Foundation (CTS99-74962), Semiconductor Research Corp. and CFD Research Corp. The authors thank Dr. Vladimir Kolobov for his insights during the course of this investigation.

[1] J. Hopwood, Plasma Sources Sci. Technol. **1**, 109 (1992).
[2] J. H. Keller, Plasma Sources Sci. Technol. **5**, 166 (1996).
[3] Z. L. Petrovic and T. Makabe, Mater. Sci. Forum **282–283**, 47 (1998).
[4] U. Kortshagen, A. Maresca, K. Orlov, and B. Heil, Appl. Surf. Sci. **192**, 244 (2002).
[5] T. Makabe and Z. L. Petrovic, Appl. Surf. Sci. **192**, 88 (2002).
[6] J. T. C. Lee *et al.*, J. Vac. Sci. Technol. A **14**, 2510 (1996).
[7] M. Tuszewski, IEEE Trans. Plasma Sci. **27**, 68 (1999).
[8] R. B. Piejak and V. A. Godyak, Appl. Phys. Lett. **76**, 2188 (2000).
[9] V. Godyak, R. Piejak, B. Alexandrovich, and A. Smolyakov, Plasma Sources Sci. Technol. **10**, 459 (2001).
[10] V. A. Godyak, R. B. Piejak, B. M. Alexandrovich, and V. I. Kolobov, Phys. Plasmas **6**, 1804 (1999).
[11] V. A. Godyak, B. M. Alexandrovich, and V. I. Kolobov, Phys. Rev. E **64**, 1 (2001).
[12] A. Sankaran and M. J. Kushner, J. Appl. Phys. **92**, 736 (2002).
[13] V. Godyak, B. Alexandrovich, R. Piejak, and A. Smolyakov, Plasma Sources Sci. Technol. **9**, 541 (2000).
[14] M. Tadokoro, H. Hirata, N. Nakano, Z. L. Petrovic, and T. Makabe, Phys. Rev. E **58**, 7823 (1998).
[15] K. Hou, S. Nakagarni, and T. Makabe, Thin Solid Films **386**, 239 (2001).
[16] R. Kinder and M. J. Kushner, J. Appl. Phys. **90**, 3699 (2001).
[17] A. V. Vasenkov and M. J. Kushner, Phys. Rev. E **66**, 066411 (2002).
[18] C. K. Birdsall and A. B. Langdon, *Plasma Physics via Computer Simulation* (McGraw-Hill, New York, 1981).
[19] V. A. Godyak and V. I. Kolobov, Phys. Rev. Lett. **79**, 4589 (1997).
[20] V. A. Godyak, R. B. Piejak, and B. M. Alexandrovich, Plasma Sources Sci. Technol. **3**, 169 (1994).
[21] S. Rauf and M. J. Kushner, J. Appl. Phys. **81**, 5966 (1997).
[22] U. Kortshagen and B. Heil, Appl. Phys. Lett. **77**, 1265 (2000).
[23] V. I. Kolobov and W. N. G. Hitchon, Phys. Rev. E **52**, 972 (1995).